Kinetic Analysis of the Characteristics of Electron Cyclotron Heating Assisted Ohmic Start-Up in the Trapped Particle Configuration of a Tokamak

Naoto TSUJII, Iwao YAMADA, Yongtae KO, Akira EJIRI, Kouji SHINOHARA, Osamu WATANABE, Seowon JANG, Yi PENG, Kotaro IWASAKI, Yuting LIN, Yuita SHIRASAWA, Taichi HIDANO, Yiming TIAN and Fumiya ADACHI

The University of Tokyo, Kashiwa 277-8561, Japan

(Received 31 January 2023 / Accepted 9 May 2023)

Electron cyclotron heating (ECH) assisted start-up is considered to be necessary for reliable start-up of tokamaks with superconducting central solenoid (CS) because of the low loop voltage. Pure Ohmic start-up using the CS requires the field-null configuration to minimize electron loss. For ECH assisted Ohmic start-up, the trapped particle configuration (TPC) was found to have wider operational parameter space than the field-null configuration experimentally. In this work, we have analyzed electron transport under the TPC using the orbit-averaged kinetic equation. The global electron distribution function was simulated by solving for the steady-state distribution function. The parameter boundary for successful pre-ionization was estimated by evaluating the net particle number growth rate from the total ionization rate and the particle flux out of the limiter boundary. Upper limit of the ECH power was predicted as that for the net particle number to grow. In the absence of the inductive electric field, the simulated high ECH power limit increased with neutral pressure and vertical field strength, consistently with the experimental results. Application of loop voltage did not change this behavior qualitatively up to the inductive electric field of 0.48 V/m, which is the typical range of low voltage start-up experiments.

Keywords: electron cyclotron heating, orbit-averaged kinetic equation, fast electron transport

DOI: 10.1585/pfr.18.1402051

1. Introduction

Tokamaks with superconducting central solenoid (CS) have low loop voltage that plasma start-up relying solely on Ohmic heating is challenging. The inductive electric field is limited to <0.3 V/m in ITER [1] and <0.5 V/m in JT-60SA [2], which is significantly smaller than present day devices (∼1.6 V/m for JT-60U, typically). Pure Ohmic start-up at the inductive electric field of 0.4 V/m has been demonstrated in DIII-D [3]. However, the minimum loop voltage was found to be sensitive to wall conditions at such low inductive electric fields. Electron cyclotron heating (ECH) assistance of Ohmic start-up has been studied to improve start-up reliability at low loop voltage [4,5]. Start-up at 0.15 V/m has been demonstrated with ECH assistance at the fundamental cyclotron resonance [4]. ECH can be used for pre-ionization also at the second harmonic resonance [6].

It has been observed that reliable Ohmic breakdown requires $E_t B_t / B_p \gtrsim 10^3$ V/m (E_t is the toroidal electric field strength, B_t is the toroidal magnetic field strength and B_p is the poloidal magnetic field strength) that puts an upper limit on the tolerable "stray" poloidal field strength for successful start-up [1]. This is understood to be because the Ohmic breakdown is a Townsend avalanche process along the magnetic field lines that requires the connection length to be sufficiently long to minimize the electron loss [7]. Such minimization of the poloidal field, i.e., the field-null configuration, is not necessary when ECH is used for pre-ionization since ECH accelerates electrons in the direction perpendicular to the magnetic field. In fact, start-up was successful at least up to the vertical field strength of ∼5 mT in the DIII-D experiment which was well above the ≲2 mT limit for pure Ohmic start-up at the same loop voltage [4]. More recently, it was found that the operational parameter space of ECH assisted Ohmic start-up can be expanded by using the trapped particle configuration (TPC) instead of the conventional field-null configuration [8–10]. The TPC has been used in non-inductive pure ECH start-up experiments to mirror-trap collisionless fast electrons [11–14]. Characteristics of ECH assisted Ohmic start-up under the TPC was observed to be similar to pure ECH start-up, which suggests that such a start-up scenario may be better described by the collisionless theory of non-inductive rf start-up [10].

In this study, we have analyzed fast electron transport during the initial phase of ECH assisted Ohmic start-up using an orbit-averaged kinetic equation. In particular, the breakdown (pre-ionization) time dependence on

author's e-mail: tsujii@k.u-tokyo.ac.jp

the ECH power and the vertical field strength was studied numerically. The organization of this paper is as follows. Section 2 describes the newly implemented orbit-averaged kinetic theory. The experimental setup is introduced in Sec. 3. The analysis of tokamak plasma breakdown is presented in Sec. 4. The discussion is given in Sec. 5 and the conclusions are given in Sec. 6.

2. Numerical Model

2.1 Orbit-averaged kinetic theory

Transport of rf generated fast particles have been described well with the orbit-averaged kinetic theory [15]. In this work, we have newly implemented an orbit-averaged kinetic equation solver to analyze fast electron transport under an equilibrium configuration without any closed flux surfaces. Finite orbit width [16] was considered to describe rf driven spatial diffusion. To perform the modeling, we used COMSOL Multiphysics ® [17].

The kinetic equation for the orbit-averaged distribution function $f(t, \mathbf{K})$ where $\mathbf{K}$ is the orbit label, is given by [16]

$$\frac{\partial f}{\partial t} = -\frac{1}{J}\frac{\partial}{\partial \mathbf{K}} \cdot (J\mathbf{\Gamma}_K), \tag{1}$$

$$\mathbf{\Gamma}_K = -\mathbf{D}_{KK} \cdot \frac{\partial f}{\partial \mathbf{K}} + \mathbf{u}_K f. \tag{2}$$

J is the absolute value of the Jacobian of the transformation from the canonical momenta to $\mathbf{K}$; $J\mathbf{dK}$ is the phase space volume of the infinitesimal volume element $\mathbf{dK}$ in canonical coordinates. $\mathbf{\Gamma}_K$ is the particle flux in $\mathbf{K}$-space expressed in terms of the orbit-averaged diffusion and convection coefficients $\mathbf{D}_{KK}$ and $\mathbf{u}_K$:

$$\mathbf{D}_{KK} = \overline{\frac{\partial \mathbf{K}}{\partial \mathbf{v}} \cdot \mathbf{D}_{vv} \cdot \frac{\partial \mathbf{k}}{\partial \mathbf{v}}}, \tag{3}$$

$$\mathbf{u}_K = \overline{\frac{\partial \mathbf{K}}{\partial \mathbf{v}} \cdot \mathbf{u}_v}. \tag{4}$$

The overlines denote orbit-averaging.

In this work, we have used $\mathbf{K} = (\mathcal{E}, \Lambda, P_\phi)$ to label electron orbits where

$$\mathcal{E} = \frac{m_e v^2}{2}, \tag{5}$$

$$\Lambda = \frac{\mu B_0}{\mathcal{E}} = \frac{B_0}{B}\frac{v_\perp^2}{v^2}, \tag{6}$$

$$P_\phi = -e\left(\psi + \frac{RB_\phi}{\Omega_e} v_\parallel\right). \tag{7}$$

Here, m_e is the electron mass, e is the elementary charge, v is the electron velocity, B is the magnetic field strength, R is the major radius, B_ϕ is the toroidal magnetic field, ψ is the poloidal flux (per radian) and $\Omega_e = -eB/m_e$ is the algebraic angular cyclotron frequency. $v_\parallel$ and $v_\perp$ are the velocity parallel and perpendicular to the magnetic field, respectively. $\mathcal{E}$ is the kinetic energy which equals the total energy in this work since we did not consider electrostatic potential. Λ is the pitch angle variable. B_0 is the toroidal field at the machine center ($R_0 = 0.36$ m in this work) introduced to make the variable Λ dimensionless. P_ϕ is the toroidal angular momentum. The absolute value of the Jacobian J for this choice of coordinates is, beside the physical and numerical constants,

$$J \propto \frac{\mathcal{E}}{\Omega_0 \omega_t}, \tag{8}$$

where $\Omega_0 = eB_0/m_e$. ω_t is the poloidal transit angular frequency defined by 2π divided by the time for the particle to complete a single poloidal orbit. To label the orbit, we also use the parallel velocity sign $\sigma = v_\parallel/|v_\parallel| = \pm 1$ as necessary.

In the present work, we considered electron transport under vertical field with positive decay index that is called the trapped particle configuration (TPC). Figure 1 shows the poloidal flux contours and the electron orbits under this poloidal field configuration. The corresponding simulation domain in K-space is shown in Fig. 2. Note in the absence of closed flux surfaces, the only closed passing orbits are the ones where parallel streaming and ∇B-drift are in the opposite directions ($\sigma = -1$ for a standard TST-2 discharge). There are two types of domain boundary. One is the boundary beyond which there is no orbit for the given $\mathbf{K}$-value. The boundary corresponds to the stagnation orbit. We imposed the no-flux boundary condition ($\mathbf{n} \cdot \mathbf{\Gamma}_K = 0$ where $\mathbf{n}$ is the vector normal to the boundary) at this boundary. The other type of the boundary is given by the orbits touching the limiter at the top, bottom, inner and outer side of the plasma. Since we consider a

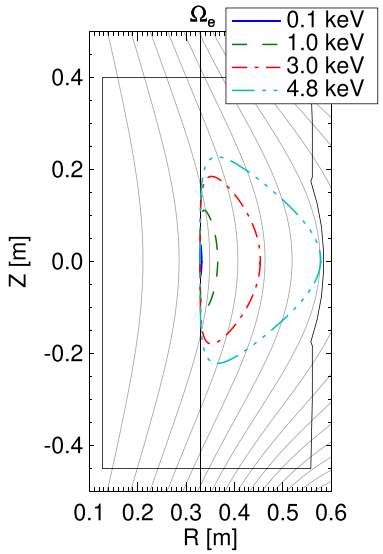

Fig. 1 The poloidal flux contours of the TPC used in this work. Electron orbits with the turning point coinciding with the EC resonance layer at midplane are also shown. The energies are for the vertical field strength of 1 mT at $R = 0.33$ m. Blue solid: 0.1 keV, green dashed: 1.0 keV, red dash-dotted: 3.0 keV, cyan dash-three-dotted: 4.8 keV. Ω_e: cyclotron resonance layer.

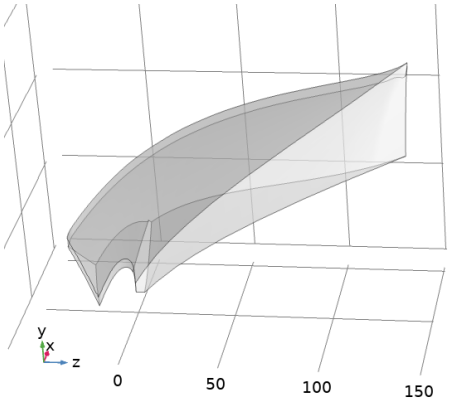

Fig. 2 The simulation domain in K-space for the TPC. $(x, y, z) = (\mathcal{E}, \Lambda, P_\phi)$.

regime where diffusive transport by ECH is dominant, the Dirichlet boundary condition with $f = 0$ was used at limiter boundaries. We have set a finite minimum energy cutoff where the distribution function was fixed at finite values with the Dirichlet boundary condition. The implication is discussed in Sec. 2.3.

2.2 Orbit-averaged transport coefficients

Electron acceleration from the room temperature during ECH breakdown requires non-linear description of wave-particle interactions [18, 19]. In this work, however, we focus on electron transport at $\gtrsim$100 eV that are expected to be better described with the conventional quasi-linear theory. To analyze breakdown in the small TST-2 device, we assume that EC waves reflect multiple times at the wall that the wave field intensity is homogeneous and the wavenumber vector and the polarization is isotropic [20]. The quasilinear diffusion coefficients are given to lowest order by (Appendix A)

$$D_{\perp\perp} = \frac{\pi e^2}{4m_e^2} A \left(1 - \frac{k_\parallel v_\parallel}{\omega}\right)^2 \frac{c}{\omega} \frac{1}{|v_\parallel|}, \tag{9}$$

$$D_{\parallel\perp} = \frac{\pi e^2}{4m_e^2} A \left(1 - \frac{k_\parallel v_\parallel}{\omega}\right) \frac{k_\parallel v_\perp}{\omega} \frac{c}{\omega} \frac{1}{|v_\parallel|}, \tag{10}$$

$$D_{\parallel\parallel} = \frac{\pi e^2}{4m_e^2} A \left(\frac{k_\parallel v_\perp}{\omega}\right)^2 \frac{c}{\omega} \frac{1}{|v_\parallel|}, \tag{11}$$

when

$$|v_\parallel| \geq \left|\frac{\omega + l\Omega_e}{k}\right|, \tag{12}$$

and zero otherwise. Here,

$$A = \frac{1}{4}\left(\frac{k_\parallel}{k} + 1\right) E_{EC}^2 J_{l-1}(z)^2, \tag{13}$$

$$k_\parallel = \frac{\omega + l\Omega_e}{v_\parallel}, \tag{14}$$

$$k_\perp = \sqrt{k^2 - k_\parallel^2}, \tag{15}$$

$$z = \frac{k_\perp v_\perp}{\Omega_e}, \tag{16}$$

c is the light speed, ω is the EC wave angular frequency and $k = \omega/c$ is the wavenumber. E_{EC} is the rms amplitude times $\sqrt{2}$ (=amplitude for monochromatic waves) of the EC waves. $J_l(z)$ is the Bessel function of the first kind and l (= 1, 2, 3, ...) is the cyclotron harmonic number.

The inductive electric field generates velocity space convection that can be introduced perturbatively with the velocity space flow

$$\mathbf{u} = -\frac{e\mathbf{E}_I}{m_e}, \tag{17}$$

where

$$\mathbf{E}_I = \frac{V_l}{2\pi R}\hat{\phi}, \tag{18}$$

is the inductive electric field, V_l is the loop voltage and $\hat{\phi}$ is the unit vector in the toroidal direction. Note that finite loop voltage implies that the poloidal flux ψ changes in time: $V_l = 2\pi\partial\psi/\partial t$. Since the P_ϕ evolution due to $v_\parallel$ acceleration and that due to the ψ evolution cancel with each other, $u_{P_\phi} = 0$ from the inductive electric field.

2.3 Breakdown characteristic analysis

We have solved for the steady-state orbit-averaged electron distribution function in the presence of ECH and inductive electric field under the initially applied poloidal field configuration. The low energy boundary of the simulation domain was set at 10 eV and the boundary value was fixed at the initial condition with the Dirichlet boundary condition. This treatment is similar to the earlier analytical work [21] where ionization was assumed to produce electrons at negligibly small energy.

Breakdown characteristics were analyzed by evaluating the global particle number growth rate using the distribution function solution. The ionization growth rate was evaluated by taking the ionization frequency moment of the distribution function. The experiment was performed with D_2, but we used H_2 ionization cross-section for the present calculations since the ionization rates for H_2 and D_2 coalesce when the average electron energy is above tens of eV [22], which was the parameter range of interest in this work. Particle flux out of the limiter boundary was taken to be the loss rate. The parameter boundary for successful breakdown was estimated from the condition where the net growth rate was high enough for the particle number to grow to a sufficiently large value within the discharge duration. That is, for breakdown to occur within the discharge duration τ,

$$\exp(\nu\tau) > G, \tag{19}$$

$$\nu > \frac{\ln G}{\tau} \equiv \nu_{thr}, \tag{20}$$

where ν is the net particle number growth rate. $G = 10^{16}$ was assumed for the results presented in this paper.

We did not consider detailed variation of the CS generated poloidal field in space and time and assumed uniform loop voltage in this work. We have also assumed that ψ was constant in time even when the loop voltage was finite, which neglected the small pinching effect that would accompany the ψ evolution in time.

3. Experimental Setup

The TST-2 spherical tokamak device (R_0 = 0.36 m, a = 0.23 m, B_{t0} < 0.3 T, I_p < 0.12 MA) is a spherical tokamak located at the University of Tokyo [23]. The CS is powered simply by discharges of capacitor banks and the waveform is fixed. The loop voltage is <5 V (inductive electric field 2.2 V/m at R_0 = 0.36 m) for typical Ohmic discharges. The machine is equipped with 5 kW ECH at 2.45 GHz. The launched polarization is X-mode for standard operation, but the EC waves reflect many times in the vessel that the launched polarization has been observed to have little effect on plasma start-up [20]. For all experimental results presented in this paper, the filling gas species was D_2 and the toroidal field strength was B_0 = 0.080 T at R_0 = 0.36 m, which placed the fundamental EC resonance layer at R_{EC} = 0.33 m.

4. Analysis of Plasma Breakdown

4.1 Fast electron transport under pure EC diffusion

We first analyzed pure EC breakdown under the TPC (Fig. 1). The simulated time evolution of the global mean energy is shown in Fig. 3. The parameters were B_0 = 0.080 T (EC resonance radius R_{EC} = 0.33 m), vertical field strength B_v = 1.0 mT (at the midplane, $R = R_{EC}$ = 0.33 m), E_{EC} = 1.0 kV/m and no loop voltage (V_l = 0 V). The initial distribution was uniform except in the $\mathcal{E}$ direction where it was 20 eV Maxwellian distribution. It can be seen that the solution is mostly converged at 0.1 ms. Here, we took the solution at 1.0 ms as the steady-state electron distribution function. The poloidal profile of the mean energy calculated from the steady-state distribution function is shown in Fig. 4. Energetic electrons in the keV range were present on the low field side of the cyclotron resonance layer. The mean electron energy was the highest near the outer limiter where electrons with large orbit width were expected to be present. The H_2 ionization rate profile is shown in Fig. 5. In contrast to the energy distribution, the ionization rate peaked strongly at the cyclotron resonance layer even

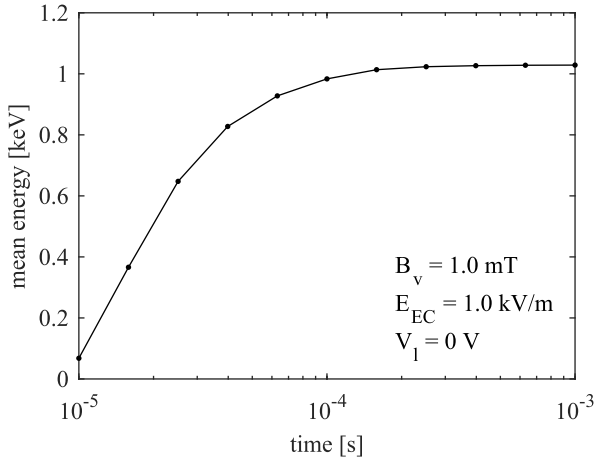

Fig. 3 The time evolution of the global mean electron energy at B_v = 1.0 mT, E_{EC} = 1.0 kV/m and V_l = 0 V.

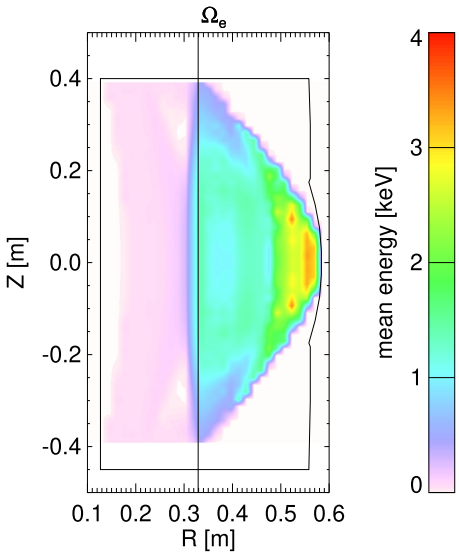

Fig. 4 The poloidal profile of the mean electron energy. B_v = 1.0 mT, E_{EC} = 1.0 kV/m and V_l = 0 V. Ω_e: cyclotron resonance layer.

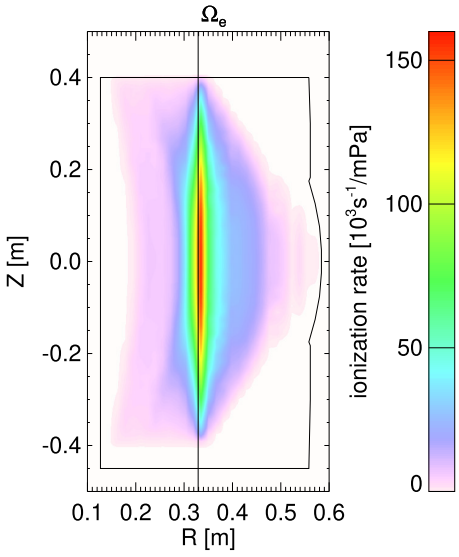

Fig. 5 The poloidal profile of the ionization rate normalized to the total number of electrons. B_v = 1.0 mT, E_{EC} = 1.0 kV/m and V_l = 0 V. Ω_e: cyclotron resonance layer.

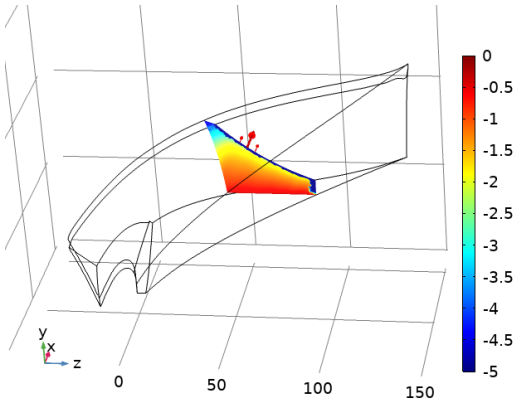

Fig. 6 The slice of electron distribution function at $\Lambda = \Lambda_c$ (colorbar, $\log_{10} f$) and the boundary loss (red arrows) in **K**-space. $(x, y, z) = (\mathcal{E}, \Lambda, P_\phi)$.

in the presence of fast electrons with large orbit deviation from the flux surfaces. The present calculation is not self-consistent because collisions including ionization were not considered in the kinetic equation. However, since ionization was strongly localized at the EC resonance where electron acceleration started, we expect the self-consistent solution to be not qualitatively different from the present solution. This point is discussed further in Sec. 5.

The electron flux out of the limiter boundary is shown with red arrows in Fig. 6. The loss was strongly localized at the critical pitch angle

$$\Lambda = \Lambda_c \equiv \frac{B_0}{B_{EC}} = \frac{\Omega_0}{\omega}, \tag{21}$$

where $B_{EC} = \omega m_e/e$ is the magnetic field strength at the EC resonance. At this pitch angle, the orbit turning point coincides with the cyclotron resonance layer, resulting in strong cyclotron interaction. The strongest acceleration path is electrons starting from around the stagnation orbit at the resonance layer (Fig. 1, blue curve), and accelerated with the turning point mostly fixed at the same location. Such an orbit evolution is shown in Fig. 1. It can be seen that 4.8 keV electrons have large orbit deviation that they intersect with the outer limiter. This is consistent with the mean energy profile of Fig. 4 that shows electron energy increasing up to ~4 keV towards the outer limiter.

The parameter boundary for successful breakdown was estimated numerically as explained in Sec. 2.3 and compared with the TST-2 experimental results. The overview of the TST-2 discharge waveforms for the EC breakdown experiments are shown in Fig. 7. ECH power was applied under constant toroidal and poloidal fields. The poloidal flux contours were shown in Fig. 1. The vertical field decay index was $-R\partial \ln B_z/\partial R = 0.47$ at $R_{EC} = 0.33$ m. Plasma generation was monitored by the visible radiation measured by the fast camera as shown in Fig. 7 (d). It can be seen that breakdown occurred more easily at *lower* ECH power at the present parameter range.

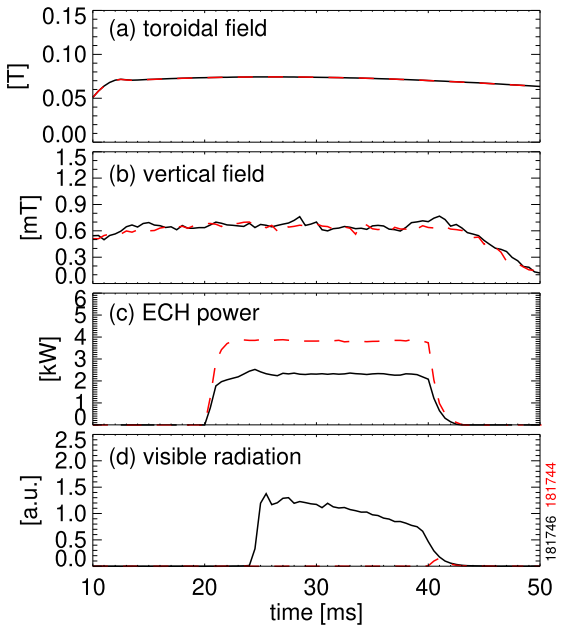

Fig. 7 Overview of the time traces of pure EC breakdown discharges. The neutral (D_2) pressure was 2.4 mPa. (a) Toroidal field strength at $R_0 = 0.36$ m (b) vertical field strength at $R_{EC} = 0.33$ m (c) ECH power (d) visible radiation measured by the fast camera. Black solid: 4 kW ECH power. Breakdown occurred around 25 ms. Red dashed: 2 kW ECH power. Breakdown did not occur within the 20 ms ECH pulse.

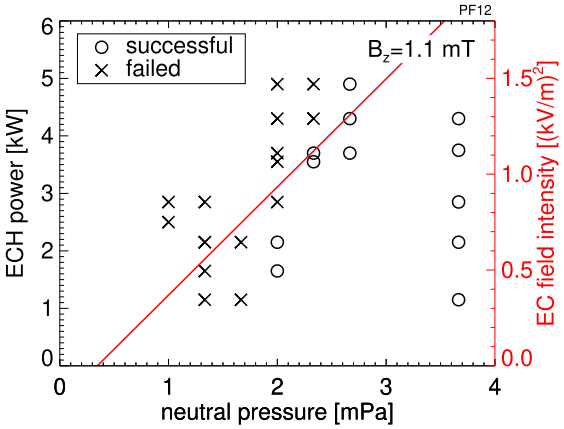

Fig. 8 The breakdown phase diagram in terms of the ECH power/field intensity and the neutral pressure. The vertical field strength was 1.1 mT and the decay index was 0.47 at $R_{EC} = 0.33$ m. Black symbols (left axis) are the experimental results and the red curve (right axis) is the simulated breakdown boundary. Circles: breakdown occurred within 10 ms, crosses: breakdown did not occur within 10 ms.

The phase diagram for successful breakdown in terms of the ECH power and the neutral pressure is shown in Fig. 8. The vertical field strength was 1.1 mT for these discharges. Discharges where breakdown occurred within 10 ms of the

start of the ECH pulse was marked as "successful". It can be seen that the high ECH power limit increased with neutral pressure. The simulated breakdown boundary is shown with the red curve in Fig. 8. The ionization cross-section for H_2 was used for the calculation as described earlier. Since D_2 ionization rate is about 6% higher at $\lesssim$9 eV [22], the breakdown boundary curve may move downwards by the same percentage at such low energy. Since the average electron energy was at least several 100 eV in the present simulation, the difference between the H_2 and D_2 ionization rates are expected to be negligible. Note the net growth rate threshold (20) for breakdown within 10 ms is $\nu_{\rm thr} = 3.7 \times 10^3\ {\rm s}^{-1}$. The simulation is in the right ballpark if we assume that 1 kW total ECH power corresponds to the EC electric field intensity ($E^2_{\rm EC}$) of 0.3 (kV/m)^2.

Figure 9 shows the breakdown phase diagram in terms of the ECH power and the vertical field strength. The numerically estimated boundary for breakdown is shown with the red curve with the same scaling as in Fig. 8 (1 kW corresponds to 0.3 (kV/m)^2). The high ECH power limit for breakdown increased at higher vertical field strength both in the simulation and the experiment. It can be seen that the high ECH power limit for breakdown increased rapidly above the vertical field strength of 0.5 mT. The maximum confined electron energy for the kind of orbits shown in Fig. 1 scales as $\mathcal{E} \propto B_{\rm v}^2$ [24]. In the simulation, the electron diffusion path became longer as the vertical field strength was increased, resulting in reduced loss and higher ECH power limit.

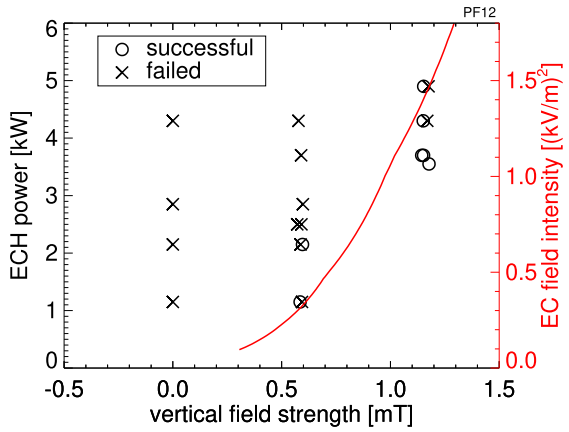

Fig. 9 The breakdown phase diagram in terms of the ECH power/field intensity and the vertical field strength. The neutral pressure was 2.5 mPa for the simulation and 2.5 ± 0.2 mPa for the experimental points. Black symbols (left axis) are the experimental results and the red curve (right axis) is the simulated breakdown boundary. Circles: breakdown occurred within 10 ms, crosses: breakdown did not occur within 10 ms.

4.2 Fast electron transport under EC diffusion and loop voltage

The impact of low loop voltage on EC breakdown was analyzed. The simulated loss and ionization rate dependence on the EC wave field intensity at the uniform and constant loop voltage of 1.0 V (0.48 V/m at $R = R_{\rm EC} = 0.33$ m) is shown in Fig. 10. It can be seen that the loss rate increased monotonically with the ECH power in the presence of loop voltage, similarly to the result without loop voltage ($V_{\rm l} = 0$) that is linear to the EC field intensity. It can be seen that the ionization rate varied little with the EC field intensity. This is because the average electron energy is in the several 100 eV range for all EC field intensities considered and the ionization rate is saturated. Breakdown is predicted to be possible only when the loss rate is sufficiently smaller than the ionization rate. The loss rate at $V_{\rm l} = 1.0$ V was smaller than that without loop voltage. This can be understood from the change in the Λ distribution shown in Figs. 11, 12. The inductive electric field drives parallel flow in the negative Λ-direction (smaller pitch angle). The effect can be seen as the change of the Λ profile of the distribution function that shows a broader peak at $\Lambda = \Lambda_{\rm c}$ with loop voltage. Because the electrons were driven off the strong ECH diffusion path at $\Lambda = \Lambda_{\rm c}$, the fast electron confinement time increased when small loop voltage was applied.

The numerically estimated breakdown boundaries were compared with the TST-2 experimental results. The overview of the TST-2 discharge waveforms for the breakdown experiments with ECH and loop voltage is shown in Fig. 13. The loop voltage was $V_{\rm l} \sim 1.0$ V. Because of the limitation in the PF coil current control system, we could keep only the vertical field strength at the constant value of 1.0 mT. The decay index was 0.47 (the value for pure EC breakdown experiments in Sec. 4.1) 4 ms af-

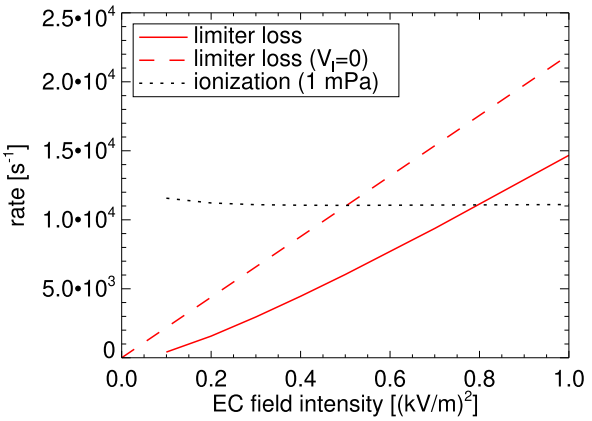

Fig. 10 The limiter loss and ionization rate dependence on the EC wave field intensity. Red solid: outer limiter loss rate at $V_{\rm l} = 1.0$ V, red dashed: outer limiter loss rate at $V_{\rm l} = 0$ V, black dotted: ionization rate at 1 mPa ($V_{\rm l} = 1.0$ V).

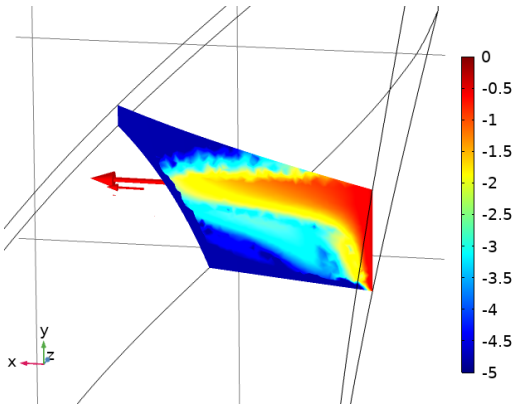

Fig. 11 The electron distribution function sliced at constant P_ϕ in **K**-space (colorbar, $\log_{10} f$) at $V_1 = 0\,\mathrm{V}$. The boundary loss is shown with the red arrows. $(x, y, z) = (\mathcal{E}, \Lambda, P_\phi)$.

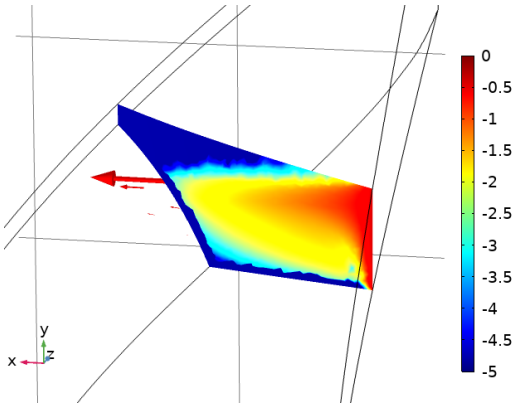

Fig. 12 The electron distribution function sliced at constant P_ϕ in **K**-space (colorbar, $\log_{10} f$) at $V_1 = 1.0\,\mathrm{V}$. The boundary loss is shown with the red arrows. $(x, y, z) = (\mathcal{E}, \Lambda, P_\phi)$.

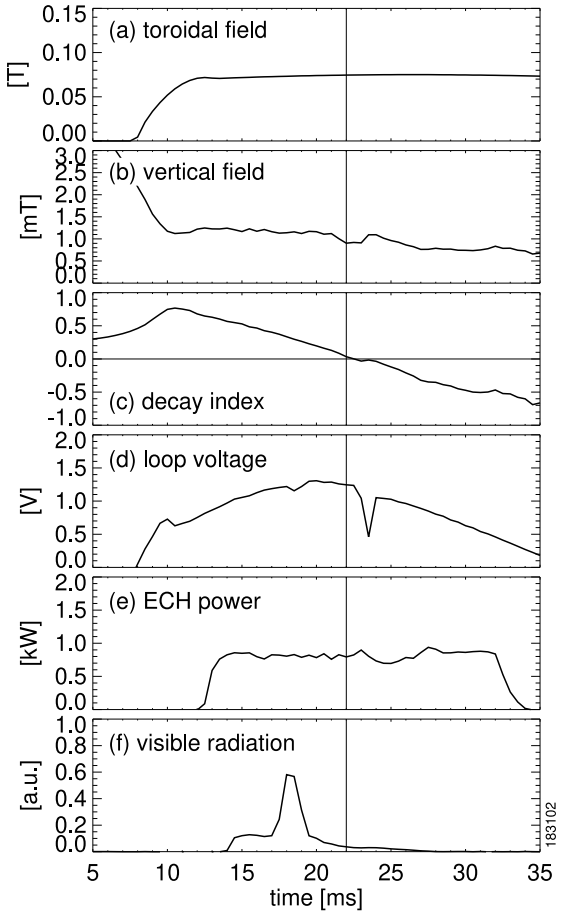

Fig. 13 Overview of the time traces of the discharge with ECH and ~1.0 V loop voltage. The neutral (D_2) pressure was 2.0 mPa. The vertical field strength was ~1.0 mT. The vertical field decay index was positive up to 22 ms indicated by the vertical lines. The visible radiation jump around 18 ms is due to closed flux surface formation. (a) Toroidal field strength at $R_0 = 0.36\,\mathrm{m}$ (b) vertical field strength at $R_{EC} = 0.33\,\mathrm{m}$ (c) vertical field decay index (d) loop voltage (e) ECH power (f) visible radiation measured by the fast camera.

ter the start of the ECH pulse and decreased to zero after 10 ms (Fig. 13 (c)). It is likely that the decreasing decay index had an effect of reducing the ECH power limit (making breakdown more difficult) than what would have been for constant decay index. The breakdown phase diagram with loop voltage in terms of the ECH power and the neutral pressure is shown in Fig. 14. It can be seen that high ECH power limit increased with neutral pressure, similarly to the case without loop voltage (Fig. 8). The simulated breakdown boundary with loop voltage is shown with the red solid curve. The simulation without loop voltage is also shown with the red dashed curve for comparison. Because convection driven by the inductive electric field reduced the loss, the high ECH power limit for breakdown was predicted to increase with loop voltage. In the experiment, however, the high ECH power limit was somewhat lower than the pure ECH case, possibly due to the suboptimal poloidal field structure in the experiment as explained above. Observation of breakdown improvement with loop voltage may require careful control of the time evolution of the poloidal field structure.

5. Discussion

The ECH breakdown characteristics were interpreted in terms of the change in the ECH driven orbit diffusion loss where the effect of loop voltage was introduced perturbatively. The effect of neutral collisions was considered only in the post-processing of the distribution function solution where the ionization rate was calculated. It may be surprising that such a simplified model could capture the experimental trend. The differential cross-section to produce electrons above $\mathcal{E} \sim 10\,\mathrm{eV}$ by impact ionizations with an H_2 molecule decreases as $\sim 1/\mathcal{E}^2$ [25]. Therefore, the electron source from ionization is expected to be concen-

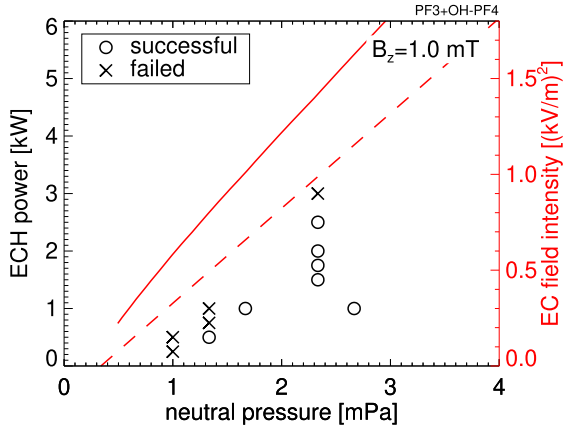

Fig. 14 The breakdown phase diagram in terms of the ECH power/field intensity and the neutral pressure with loop voltage. The loop voltage was 1.0 V and the vertical field strength was 1.0 mT (at R_{EC} = 0.33 m) in the simulation. The values for the experiment are shown in Fig. 13. Black symbols (left axis) are the experimental results and the red solid curve (right axis) is the simulated breakdown boundary at V_l = 1.0 V. The red dashed curve shows that without loop voltage (V_l = 0) for comparison. Circles: breakdown occurred within 10 ms, crosses: breakdown did not occur within 10 ms.

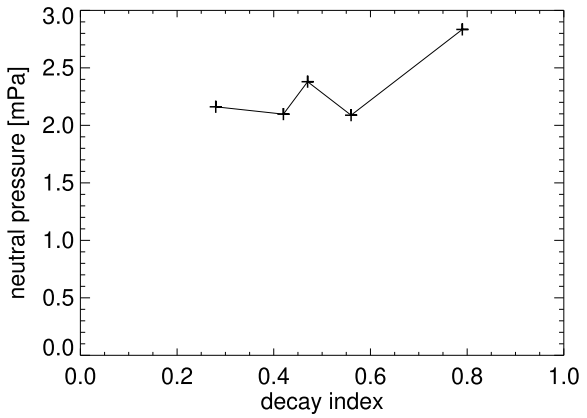

Fig. 15 The simulated breakdown threshold neutral pressure at the vertical field decay index of 0.28 (PF2:PF3=9:1), 0.42 (PF2), 0.47 (PF2:PF3=1:1), 0.56 (PF1:PF2=8:2) and 0.79 (PF1). The ECH field intensity was 1 (kV/m)^2, the loop voltage was 1.0 V, and the vertical field strength was 1.0 mT (at R_{EC} = 0.33 m).

trated at $\lesssim$10 eV. In addition, nonlinear ECH [18, 19] is expected to easily accelerate electrons produced at $\lesssim$10 eV to above the ionization energy. As long as we can assume that ~10 eV electrons are always present around the cyclotron resonance layer (Fig. 5), the mean energy of electrons is expected to be well above the ionization energy in the high ECH power and low neutral pressure regime. At such a condition, the net ionization rate is saturated near the maximum value that it varies little with parameter change (Fig. 10, black dotted curve). If the dominant transport loss channel in the TPC is the ECH driven orbit diffusion loss, the present model would capture the experimental trend. Neutral collisions may decrease the loss rate by moving the electrons off the strong ECH diffusion path, or increase the loss rate by scattering the electrons into the loss orbits. In either case, the collisional effect is expected to become subdominant in the high ECH power and low neutral pressure regime, which is of our primary interest in the present work. This is in contrast to pure Ohmic breakdown where the mean electron energy is around the H_2 ionization energy of 15.4 eV at parameters near the breakdown boundary, especially at low loop voltage. Detailed neutral collision dynamics, including elastic scattering, excitation and ionization, is of critical importance under such a condition.

Experimentally, the positive effect of vertical field was not observed at very small decay index (~0.05) [10]. This can be understood to be because of the vanishingly thin closed-orbit domain in the Λ-direction. Such a dependence cannot be simulated quantitatively accurately with the present simulation since collisions are neglected and electron transport in the Λ-direction is likely underpredicted. Figure 15 shows the simulated dependence of the breakdown threshold pressure on the vertical field decay index. It can be seen that the threshold pressure depends only weakly on the decay index. This was because electron transport was mostly in the energy direction and steady-state was reached when the EC wave diffusion and losses from the outer limiter was balanced; the closed-orbit domain structure and transport in the Λ-direction did not matter. The threshold pressure increased slightly at higher decay index in this model. The scan was performed with the vertical field strength at the EC resonance (R = 0.33 m) fixed, so for higher decay index, the vertical field was weaker on the low-field side of the EC resonance. This resulted in greater orbit expansion at higher energy for high decay index that led to higher loss and higher threshold pressure. At the smallest decay index, top/bottom limiter losses start to increase, but the present model may not be quantitatively accurate in this parameter range. Overall, as long as the decay index is greater than ~0.3, we expect that the breakdown characteristics do not depend strongly on the decay index.

The present work shows that application of the vertical field with the correct structure (positive decay index, i.e., TPC) is beneficial for breakdown. Theoretically, there is no upper limit to the vertical field strength, as long as convection by the inductive electric field is subdominant to ECH diffusion. This is not surprising considering the fact that ECH is routinely used for plasma production in stellerators [18]. In a tokamak, however, closed flux surface formation at low plasma current prefers low vertical field strength. High vertical field strength is not only unnecessary, but detrimental since it delays closed flux surface formation. In a pure Ohmic start-up, the optimum ver-

tical field strength has been observed to be around ~0.5 mT in the direction required for force balance of the plasma current [4]. The optimum vertical field strength for an ECH assisted start-up depends on the machine size and the ECH power, but it is not expected to be much higher than a few mT since keV electrons are already confined at this value under the TPC.

6. Conclusions

The global electron distribution function during breakdown under the open field-line trapped particle configuration (TPC) was obtained by solving for the steady-state solution of the orbit-averaged kinetic equation. Diffusive transport driven by ECH and convective transport driven by inductive electric field was considered. The boundary for successful breakdown was estimated by evaluating the global ionization rate and the transport loss rate out of the limiter using the steady-state distribution function solution. The high ECH power limit for breakdown increased linearly with neutral pressure for pure ECH breakdown. The dominant loss channel was ECH driven orbit diffusion out of the outer limiter. The electron acceleration path started from a stagnation orbit at the EC resonance layer. The electron orbit expanded to the low-field side while the orbit turning point mostly stayed at the EC resonance layer, until the orbit intersected with the outer limiter where the electrons were lost. Increasing the vertical field strength increased the maximum energy of the confined electrons, which, in turn, increased the ECH power limit. These simulated trends were consistent with the TST-2 experimental results. Application of loop voltage in the simulation did not qualitatively change the breakdown characteristics from the pure EC breakdown case for the inductive electric field of up to 0.48 V/m, which is the typical range of low voltage Ohmic start-up experiments. The numerical simulation showed that the loss rate was smaller with loop voltage since the electrons were convected off the strong ECH acceleration path along the critical pitch angle. In the experiment, on the other hand, breakdown was slightly more difficult with loop voltage but this may be due to the suboptimal poloidal field structure.

Appendix A. The EC Quasilinear Diffusion Coefficients

At non-relativistic velocities, the quasilinear diffusion coefficients for species with charge q and mass m are given by [26]

$$D_{\perp\perp} = \frac{\pi q^2}{m^2}\frac{1}{2}\int \frac{\mathrm{d}\mathbf{k}}{(2\pi)^3}\frac{|\psi_k|^2}{V}\left(1-\frac{k_\parallel v_\parallel}{\omega}\right)^2 \cdot \delta(\omega - k_\parallel v_\parallel - l\Omega), \tag{A.1}$$

$$D_{\parallel\perp} = D_{\perp\parallel} = \frac{\pi q^2}{m^2}\frac{1}{2}\int \frac{\mathrm{d}\mathbf{k}}{(2\pi)^3}\frac{|\psi_k|^2}{V}\frac{k_\parallel v_\perp}{\omega}\left(1-\frac{k_\parallel v_\parallel}{\omega}\right) \cdot \delta(\omega - k_\parallel v_\parallel - l\Omega), \tag{A.3}$$

$$D_{\parallel\parallel} = \frac{\pi q^2}{m^2}\frac{1}{2}\int \frac{\mathrm{d}\mathbf{k}}{(2\pi)^3}\frac{|\psi_k|^2}{V}\left(\frac{k_\parallel v_\perp}{\omega}\right)^2 \cdot \delta(\omega - k_\parallel v_\parallel - l\Omega), \tag{A.4}$$

where, for monochromatic frequency,

$$\frac{1}{2}\int \frac{\mathrm{d}\mathbf{k}}{(2\pi)^3}\frac{|E_k|^2}{V} = \langle E^2\rangle. \tag{A.5}$$

We take the z-axis in the background magnetic field direction, the wavenumber to be in the x-z plane and $\hat{y} = \hat{z}\times\hat{x}$. Defining the wave propagation direction θ as $\mathbf{k}\cdot\mathbf{B}/B = \cos\theta$ and the linear polarization angle from the x-axis as α, the electric field can be written

$$E_k \propto \begin{pmatrix} \cos\alpha\cos\theta \\ \sin\alpha \\ -\cos\alpha\sin\theta \end{pmatrix}. \tag{A.6}$$

For an isotropic wavenumber spectrum with $k = \omega/c$, the E^- (right hand circularly polarized electric field) integral term becomes

$$\frac{1}{2}\int \frac{\mathrm{d}\mathbf{k}}{(2\pi)^3}\frac{|E_k^-|^2}{V} \tag{A.7}$$

$$\to \mathcal{N}\frac{1}{2}\int \frac{\mathrm{d}\alpha}{2\pi}\frac{\mathrm{d}\mathbf{k}}{(2\pi)^3}\delta\left(k-\frac{\omega}{c}\right) \cdot \frac{1}{2}(\cos^2\alpha\cos^2\theta + \sin^2\alpha). \tag{A.8}$$

The normalization $\mathcal{N}$ can be written in terms of the electric field amplitude E_{EC}

$$\mathcal{N}\frac{1}{2}\int \frac{\mathrm{d}\alpha}{2\pi}\frac{\mathrm{d}\mathbf{k}}{(2\pi)^3}\delta\left(k-\frac{\omega}{c}\right) = \langle E^2\rangle = \frac{E_{\mathrm{EC}}^2}{2}. \tag{A.9}$$

Noting $\mathrm{d}\mathbf{k} = 2\pi k^2 \mathrm{d}k\,\mathrm{d}(\cos\theta)$, we obtain

$$D_{\perp\perp} = \frac{\pi e^2}{4m_{\mathrm{e}}^2}A\left(1-\frac{k_\parallel v_\parallel}{\omega}\right)^2\frac{c}{\omega}\frac{1}{|v_\parallel|}, \tag{A.10}$$

$$D_{\parallel\perp} = \frac{\pi e^2}{4m_{\mathrm{e}}^2}A\left(1-\frac{k_\parallel v_\parallel}{\omega}\right)\frac{k_\parallel v_\perp}{\omega}\frac{c}{\omega}\frac{1}{|v_\parallel|}, \tag{A.11}$$

$$D_{\parallel\parallel} = \frac{\pi e^2}{4m_{\mathrm{e}}^2}A\left(\frac{k_\parallel v_\perp}{\omega}\right)^2\frac{c}{\omega}\frac{1}{|v_\parallel|}, \tag{A.12}$$

when

$$\left|\frac{\omega + l\Omega_{\mathrm{e}}}{k v_\parallel}\right| = |\cos\theta| \le 1, \tag{A.13}$$

and zero otherwise. A is as defined in the main section.

[1] Y. Gribov, D. Humphreys, K. Kajiwara, E.A. Lazarus, J.B. Lister, T. Ozeki, A. Portone, M. Shimada, A.C.C. Sips and J.C. Wesley, Nucl. Fusion **47**, S385 (2007).

[2] H. Urano, T. Fujita, S. Ide, Y. Miyata, G. Matsunaga and M. Matsukawa, Fusion Eng. Des. **100**, 345 (2015).

[3] E.A. Lazarus, A.W. Hyatt, G.L. Jackson and D.A. Humphreys, Nucl. Fusion **38**, 1083 (1998).

[4] B. Lloyd, G.L. Jackson, T.S. Taylor, E.A. Lazarus, T.C. Luce and R. Prater, Nucl. Fusion **31**, 2031 (1991).
[5] K. Kajiwara, Y. Ikeda, M. Seki, S. Moriyama, T. Oikawa, T. Fujii and JT-60 Team, Nucl. Fusion **45**, 694 (2005).
[6] G.L. Jackson, J.S. deGrassie, C.P. Moeller and R. Prater, Nucl. Fusion **47**, 257 (2007).
[7] A. Ejiri, Y. Takase, N. Tsujii, S. Yajima, H. Yamazaki and O. Mitarai, Nucl. Fusion **60**, 036015 (2020).
[8] Y.H. An, J. Lee, J.G. Jo, B.-K. Jung, H.Y. Lee, K.-J. Chung, Y.-S. Na, T.S. Hahm and Y.S. Hwang, Nucl. Fusion **57**, 016001 (2016).
[9] J. Lee, J. Kim, Y.H. An, M.-G. Yoo, Y.S. Hwang and Y.-S. Na, Nucl. Fusion **57**, 126033 (2017).
[10] Y. Ko, N. Tsujii, Y. Takase, A. Ejiri, O. Watanabe, H. Yamazaki, K. Iwasaki, P. Yi, J.H.P. Rice, Y. Osawa, T. Wakatsuki, M. Yoshida and H. Urano, Plasma Fusion Res. **16**, 1402056 (2021).
[11] C.B. Forest, Y.S. Hwang, M. Ono, G. Greene, T. Jones, W. Choe, M. Schaffer, A. Hyatt, T. Osborne, R.I. Pinsker, C.C. Petty, J. Lohr and S. Lippmann, Phys. Plasmas **1**, 1568 (1994).
[12] M. Uchida, T. Yoshinaga, H. Tanaka and T. Maekawa, Phys. Rev. Lett. **104**, 065001 (2010).
[13] A. Ejiri, Y. Takase, H. Kasahara, T. Yamada, K. Hanada, K.N. Sato, H. Zushi, K. Nakamura, M. Sakamoto, H. Idei, M. Hasegawa, A. Iyomasa, N. Imamura, K. Esaki, M. Kitaguchi, K. Sasaki, H. Hoshika, O. Mitarai and N. Nishino, Nucl. Fusion **46**, 709 (2006).
[14] T. Maekawa, T. Yoshinaga, M. Uchida, F. Watanabe and H. Tanaka, Nucl. Fusion **52**, 083008 (2012).
[15] J.C. Wright, A. Bader, L.A. Berry, P.T. Bonoli, R.W. Harvey, E.F. Jaeger, J.-P. Lee, A. Schmidt, E. D'Azevedo, I. Faust, C.K. Phillips and E. Valeo, Plasma Phys. Control. Fusion **56**, 045007 (2014).
[16] Y.V. Petrov and R.W. Harvey, Plasma Phys. Control. Fusion **58**, 115001 (2016).
[17] COMSOL Multiphysics ® www.comsol.com. COMSOL AB, Stockholm, Sweden.
[18] M.D. Carter, D.B. Batchelor and A.C. England, Nucl. Fusion **27**, 985 (1987).
[19] D. Farina, Nucl. Fusion **58**, 066012 (2018).
[20] J. Sugiyama, A. Ejiri, Y. Takase, O. Watanabe, Y. Adachi, H. Tojo, M. Sasaki, T. Masuda, T. Oosako and S. Kainaga, Plasma Fusion Res. **3**, 026 (2008).
[21] A.D. Macdonald and S.C. Brown, Phys. Rev. **76**, 1634 (1949).
[22] D.J. Rose, Phys. Rev. **104**, 273 (1956).
[23] Y. Takase, A. Ejiri, N. Kasuya, T. Mashiko, S. Shiraiwa, L.M. Tozawa, T. Akiduki, H. Kasahara, Y. Nagashima, H. Nozato, H. Wada, H. Yamada, T. Yamada and K. Yamagishi, Nucl. Fusion **41**, 1543 (2001).
[24] A. Ejiri and Y. Takase, Nucl. Fusion **47**, 403 (2007).
[25] T.W. Shyn, W.E. Sharp and Y.-K. Kim, Phys. Rev. A **24**, 79 (1981).
[26] T.H. Stix, *Waves in Plasmas* (American Institute of Physics, New York, 1992).